



Enhancing promoting effects in g-C₃N₄-Mⁿ⁺/CeO₂-TiO₂ ternary composites: Photo-handling of charge carriers

Mario J. Muñoz-Batista^a, Maxim A. Nasalevich^b, Tom J. Savenije^c, Freek Kapteijn^b, Jorge Gascon^{b,*}, Anna Kubacka^{a,**}, Marcos Fernández-García^a

^a Instituto de Catálisis y Petroleoquímica, CSIC, Marie Curie 2, 28049 Madrid, Spain

^b Catalysis Engineering, Department of Chemical Engineering, Delft University of Technology, Julianalaan 136, Delft, The Netherlands

^c Optoelectronic Materials, Department of Chemical Engineering, Delft University of Technology, Julianalaan 136, Delft, The Netherlands

ARTICLE INFO

Article history:

Received 27 February 2015

Received in revised form 13 April 2015

Accepted 24 April 2015

Available online 27 April 2015

Keywords:

Photocatalysis

Mineralization

Titania

Ceria

Carbon nitride

ABSTRACT

The promotion of a TiO₂ photocatalyst by surface species consisting of cerium oxide and metal-promoted carbon nitride (g-C₃N₄) was analyzed to gain insight into the effect of Ca or Fe cationic species of the carbon nitride component in the overall performance of the photocatalytic system. The resulting materials were characterized with X-ray diffraction, time-resolved microwave conductivity (TRMC) and photoelectron, infrared, UV–visible and photoluminescence spectroscopies. The photoactivity of the materials in the gas phase elimination of toluene was evaluated under UV and sunlight-type illumination conditions and the corresponding true reaction quantum efficiency values calculated. The photoluminescence and TRMC analyses provide unequivocal evidence that the presence of Fe and Ca alter charge recombination to a different degree, leading to qualitatively different, promoting photochemical effects. This occurs exclusively in co-presence of ceria species at the titania surface and is thus characteristic of the ternary composite heterostructures.

© 2015 Elsevier B.V. All rights reserved.

1. Introduction

Nano-sized titanium oxide(s) and, particularly the anatase polymorph is the universal photocatalyst due to its chemical versatility, high activity and low cost derived from relatively cheap raw elements as well as a modest operation cost in optimum conditions, requiring neither energy (temperature, pressure) nor reactants (oxidant) inputs [1–4]. The use of anatase has however frequently being applied in combination with other phases, typically in relatively small quantities in order to avoid shadowing effects at the titania surface and a subsequent negative impact on photocatalytic properties. These phases can have adequate physico-chemical properties to enhance photoactivity within a variety of situations concerning light wavelength in the UV/Visible/IR regions and/or the different chemical nature (like polar or nonpolar) of the reactants. Most broadly attempted phases favor the efficient separation of electron and hole charge carriers and the subsequent decrease of charge recombination. Other modifiers are introduced in the catalyst formulation aiming at enhancement of light absorption

properties, particularly in the visible region where anatase has a relatively limited performance. Both aims can be accomplished simultaneously within a general strategy to optimize the performance of TiO₂-based materials using composite catalysts [1–6].

Composite catalysts are usually binary systems but in recent dates ternary or more complex systems have been essayed [2–6]. In this contribution we combine a dominant (by weight percentage) anatase component with two semiconductors of different chemical nature. The first one is cerium oxide. The contact between ceria and titania is known to provide rather active materials independently of the excitation wavelength [2,7]. It has been applied for the elimination of organic pollutants through reduction and/or oxidation reactions [8–26] and, very recently, for the inactivation of microorganisms [16,20]. The second is the g-C₃N₄-based carbon nitride. Similarly to the ceria case, the combination with titania has been shown to provide outstanding photochemical activity in a number of reactions such as hydrogen production [27–30] or CO₂ reduction [31], as well as in a series of degradation reactions concerning several pollutants such as formaldehyde [32], phenol [33], toluene [34], organic dyes [35–41] as well as the removal of Cr(VI) [35]. The use of both surface modifiers in contact with titania has been also studied in one of our previous works, providing information concerning the optimum loading of both phases while used simultaneously [42].

* Corresponding author. Tel.: +31 (0) 15 2789820; fax: +31 (0) 15 2785006.

** Corresponding author. Tel.: +34 91 585 4939; fax: +34 91 585 4760.

E-mail addresses: J.Gascon@tudelft.nl (J. Gascon), ak@icp.csic.es (A. Kubacka).

The effectiveness of the combination of the cerium and carbon nitride species at the titania-anatase surface has been shown, on the other hand, to be influenced to an important degree by simple manganese cationic species sited at the interface between the carbon nitride and the titania phases [43]. This happens with rather minute concentrations (at the level of 10^{-2} mol.% in the catalyst) of the cationic species. To study the generality of this trend, here we analyze two promoters chosen from a previous screening using five elements (Ca, Cr, Fe, Mn, and Zr). Two different situations were encountered. As it will be detailed hereafter, the first, with Ca as characteristic example, has positive effects whereas the second, with Fe as illustrative example, has mild positive or neutral effects in the UV and sunlight-type photo-degradation of toluene, a typical pollutant present in urban atmospheres and demanding highly active photocatalysts for its elimination [44–47].

To provide a rigorous, quantitative analysis of the photoactivity and thus to study the Ca or Fe on the system performance, we will first present results based on quantum efficiency calculations under all illumination conditions here reported. Calculating quantum efficiency of a reaction involves, in first place, measurements and modelling of the radiation reaching the surface of a given material and the fraction of light effectively used in photocatalytic steps. Such task typically requires experimental and modeled light source emission properties and, subsequently, the light absorption capability of the photocatalysts. The whole process requires to solve the so-called radiative transfer equation, by calculating in our case the so-called local superficial rate of photon absorption ($e^{a,s}$) [13,48–51]. In second place, the accurate calculation of the quantum efficiency requires taking into account the number of charge carriers used for each specific chemical product of the reaction [34,42].

In addition and with the aim of interpreting the quantum efficiency results on physico-chemical basis we carried out a multitechnique examination of the materials using X-ray diffraction, photoelectron, infrared, photoluminescence and ultraviolet spectroscopies and TRMC to interpret the ternary system behavior as a function of the Ca or Fe species under UV and visible light illumination conditions. After a basic characterization showing that both Ca and Fe containing TiO_2 -based ternary systems are structurally similar to the corresponding single and binary reference samples, the influence of the cation on the photoactivity is evidenced by a combination of photoluminescence and TRMC analysis. We essentially observed that the photoactive behavior is directly linked to the effect of Ca/Fe cations on charge handling properties of the corresponding solids.

2. Materials and methods

2.1. Catalyst preparation

Materials were prepared using a microemulsion preparation method using *n*-heptane (Scharlau) as an organic media, Triton X-100 (Aldrich) as a surfactant and hexanol (Aldrich) as a co-surfactant. TiO_2 reference sample was obtained in the first step using titanium tetraisopropoxide as the titanium precursor. In the CeO_2 - TiO_2 , and CeO_2 reference, cerium nitrate (Alfa Aesar) was introduced into the aqueous phase of a microemulsion. After 30 min of agitation, a stoichiometric quantity of tetramethylammonium-hydroxide (TMAH) was introduced from the aqueous phase of a similar microemulsion to obtain 2.5 mol.% of Ce(III) hydroxide. After 5 min, titanium tetraisopropoxide was added to the resulting microemulsion dropwise from a mixture with isopropanol (2:3). Water/(Ti+Ce) and water/surfactant molar ratios were, 110 and 18 for all samples [52,53]. The resulting mixture was stirred for 24 h, centrifuged, and the separated solids rinsed with methanol

and dried at 110°C for 12 h. After drying, the solid precursors were subjected to a heating ramp of 2°C min^{-1} up to 500°C and then the temperature was maintained for 2 h.

The graphitic carbon nitride ($\text{g-C}_3\text{N}_4$) was obtained by calcination of melamine (Aldrich) at 580°C for 4 h with a heating ramp of 5°C min^{-1} . To obtain the cation-modified carbon nitride, Ca/Fe precursors (Ca(II) and Fe(II) chlorides, Aldrich) were dissolved in deionized water to produce a 10 mM solution. Then, the salt precursor solution was added to 200 mL of a 0.5 mg mL^{-1} uniformly dispersed $\text{g-C}_3\text{N}_4$ aqueous suspension. The mixture was kept under stirring for 1 h at room temperature. Afterwards, the solution was centrifuged and thoroughly washed with deionized water followed by drying at 60°C .

The incipient wetness impregnation method was used to obtain the $\text{g-C}_3\text{N}_4$ -M/ CeO_2 - TiO_2 (M = Ca, Fe) ternary composites. For this purpose, $\text{g-C}_3\text{N}_4$ was suspended in methanol to obtain ca. 1 mol. % suspension and sonicated for 1 h, deposited on the CeO_2 - TiO_2 composite sample and dried at 110°C for 24 h. Sample names are Ti, CeTi and g for the TiO_2 , CeO_2 - TiO_2 and $\text{g-C}_3\text{N}_4$ references, respectively. We also used g-M/Ti and g-M/CeTi names for, respectively, $\text{g-C}_3\text{N}_4$ -M/ TiO_2 and $\text{g-C}_3\text{N}_4$ -M/ CeO_2 - TiO_2 composite samples, where M = Ca or Fe. The composition of the materials was analyzed using ICP-AAS.

2.2. Experimental techniques

The Brunauer–Emmett–Teller (BET) surface areas and average pore volumes and sizes were measured by nitrogen physisorption (Micromeritics ASAP 2010). The specific surface areas were determined by application of the BET equation [54]. Mesopore volumes were determined from the amount adsorbed at a relative pressure of 0.96 on the desorption branch of the isotherm. XRD profiles were obtained with a Seifert D-500 diffractometer using Ni-filtered $\text{Cu K}\alpha$ radiation with a 0.02° step and fitted using the Von Dreele approach to the Le Bail method [55]; particle sizes and microstrain were measured with XRD using the Williamson–Hall formalism [56]. UV–vis transmission or diffuse-reflectance spectroscopy experiments were performed with a Shimadzu UV2100 apparatus using BaSO_4 as a white standard in the case of the reflectance mode experiments. TEM analysis of the materials was carried out with a JEOL 2100F TEM/STEM microscope. X-ray energy dispersive spectra (XEDS) analysis was performed in STEM mode, with a probe size $\sim 1 \text{ nm}$, using the INCA x-sight (Oxford Instruments) detector. The Fourier transform infrared spectra were taken on a Bruker Vertex 80 FTIR spectrometer using an MCT detector. XPS data were recorded on $4 \times 4 \text{ mm}^2$ pellets, 0.5 mm thick, prepared by gentle pressing of the powdered materials which were outgassed in the pre-chamber of the instrument at room temperature down to a pressure of $< 2 \times 10^{-8}$ Torr to remove chemisorbed water from the surfaces. The SPECS spectrometer main chamber, working at a pressure of $< 10^{-9}$ Torr, was equipped with a PHOIBOS 150 multichannel hemispherical electron analyser with a dual X-ray source working with $\text{Ag K}\alpha$ ($h\nu = 1486.2 \text{ eV}$) at 120 W, 20 mA using C 1s as the energy calibration reference (284.6 eV). Surface chemical compositions were estimated from XPS spectra, by calculating the integral of each peak after subtraction of the “S-shaped” Shirley-type background using appropriate experimental sensitivity factors and the CASA-XPS (version 2.3.15) software. Steady-state emission spectra were acquired using a QuantaMaster QM-1 (PTI). 100 W Xenon arc lamp (200–900 nm) was used as a light source equipped with 121A excitation double monochromators. Model MP-1 sample compartment, 101A emission monochromator, Model 710 photon counting detector PMT (185–900 nm) completed the experimental setup.

TRMC probes a change in conductance induced by light. This change represents the product of charge generation efficiency and the charge carriers' mobility. In a typical experiment a sample is

excited with a laser pulse and mobile charge carriers are probed with microwaves. These experiments were performed at a dedicated homebuilt setup. For a complete description one is referred to refs. [57,58]. Excitation of the sample was achieved by 340 and 420 nm laser light pulses of a Q-switched Nd:YAG laser (“Vibrant II”, Opotek). The laser was employed to pump an optical parametric oscillator (OPO) efficiencying 3 ns fwhm pulses. The experiments were carried out at the full light intensity of 1.9×10^{14} incident photons/cm² in the case of 340 nm excitation and 3.2×10^{16} incident photons/cm² in the case of 420 nm.

2.3. Photocatalytic experimental details

Gas-phase photo-oxidation of toluene (Panreac, spectroscopic grade) was carried out in a continuous flow annular photoreactor using a set-up described elsewhere [13,59,60]. Activity and selectivity of the gas-phase photooxidation were tested using 40 mg of photocatalyst as a thin layer coated on the annular photoreactor. The indicated amount of catalyst was suspended in 1 mL of ethanol, painted on a pyrex tube (cut-off at ca. 290 nm), and dried at room temperature. The reacting mixture (100 mL/min) was prepared by injecting toluene ($\geq 99\%$; Aldrich) into a wet (ca. 75% relative humidity) 20 vol.% O₂/N₂ flow before entering to the photoreactor, efficiencying an organic inlet concentration of ca. 700 ppmv. Under such conditions, the reaction rate shows a zero-order kinetics with respect to the total flow and organic pollutant/oxygen concentrations. After feeding the mixture for 6 h (control test) in the dark, the catalyst was irradiated by four fluorescent daylight lamps (6 W, Sylvania F6W/D) with a radiation spectrum simulating sunlight (UV content of 3%; main emission lines at 410, 440, 540, and 580 nm, symmetrically positioned outside the photoreactor (Fig. A1). Similar tests were carried out using UV lamps (Sylvania F6WBLT-65; 6W, maximum at ca. 350 nm). Reaction rates were evaluated (*vide supra*) under steady-state conditions, typically achieved after ca. 6–10 h of irradiation. No change in activity was detected for all samples within the next 24 h. The concentration of reactants and products was analyzed using an on-line gas chromatograph (Agilent GC 6890) equipped with HP-PLOT-Q/HP-Innowax columns (0.5/0.32 mm I.D. \times 30 m) and TCD (for CO₂ measurement)/FID (organic measurement) detectors. The carbon balance was $>95\%$ in all experiments.

3. Results and discussion

3.1. Characterization

Reference and sample chemical compositions are presented in Table 1. The g-M/Ti references have a M content very close to 1 weight % in both Ca and Fe cases. In the ternary systems, ceria is present in a 5.8–5.9 weight % (2.9–3 mol. %) while carbon nitride is at 1 weight%. This means that the M content in the ternary catalysts is around 10^{-2} mol.% level. The constancy of the surface ceria and

Table 1
Sample Chemical Compositions (weight).^a

Sample	Ca or Fe	g-C ₃ N ₄	CeO ₂	TiO ₂
g-Ca	0.01	0.99	-	-
g-Fe	0.01	0.99	-	-
g/Ti	-	0.01	-	0.99
g-Ca/Ti	n.d.	0.009	-	0.991
g-Ca/CeTi	n.d.	0.009	0.058	0.932
CeTi	-	-	0.059	0.931
g/CeTi	-	0.009	0.058	0.932
g-Fe/Ti	n.d.	0.009	-	-
g-Fe/CeTi	n.d.	0.009	0.058	0.932

^a n.d.: not determined. Maximum standard error: 4%.

Table 2
Band gap and morphological properties of the samples.

Sample	Band gap (eV)	BET surface area (m ² g ⁻¹)	Pore volume (cm ³ g ⁻¹)	Pore size (nm)
Ti	3.20	95.8	0.123	5.2
g/Ti	3.12	97.2	0.112	4.6
CeTi	2.97	100.7	0.112	4.2
g/CeTi	2.94	101.0	0.112	4.1
g-Fe/Ti	3.12	95.8	0.111	4.4
g-Fe/CeTi	2.95	100.0	0.111	4.0
g-Ca/Ti	3.12	96.1	0.111	4.5
g-Ca/CeTi	2.94	99.6	0.110	3.9

a) Standard error: band gap 0.04 eV, BET 1.5 m² g⁻¹; pore size 8%.

carbon nitride species content within the ternary samples series is demonstrated by chemical analysis.

The basic physico-chemical characterization results for references and samples are summarized in Table 2. Starting with the surface area, our TiO₂ reference possesses a surface area of ca. 95.8 m² g⁻¹. This value increases by ca. 5 m² g⁻¹ in the presence of CeO₂ while the subsequent addition of g-C₃N₄ does not significantly modify the surface area. If compared with the carbon nitride reference we thus observed that the surface area is dominated by the major titania component with a modest (ca. 5%) positive effect of CeO₂ and a nearly negligible influence of g-C₃N₄. As expected, the presence of Ca or Fe in the catalyst formation does not affect the surface area (Table 2). All such conclusions can be extended to the interpretation of other morphological properties as demonstrated by the pore volumes and sizes reported in Table 2.

The X-ray diffraction patterns of the g-M/CeTi samples and the corresponding single and binary reference systems are shown in Fig. 1. The comparison of the patterns makes obvious the exclusive presence of anatase (JCPDS card 78-2486, corresponding to the I4₁/amd space group). Table 3 lists the data for the anatase primary particle size, strain and cell parameters. In Fig. 1, the g-C₃N₄ and g-C₃N₄-M nanomaterials XRD profiles are dominated by the interlayer-stacking (002) reflection. As expected due to their limited weight percentage, no evidence of Ca²⁺ and Fe²⁺ presence is obtained using XRD.

Summarizing the results in Tables 2 and 3, in our case the presence of surface species can alter the main titania component morphological and structural properties as a function of the degree of interaction allowed by the preparation method. Ceria is produced in a single pot step with titania and thus its presence affects

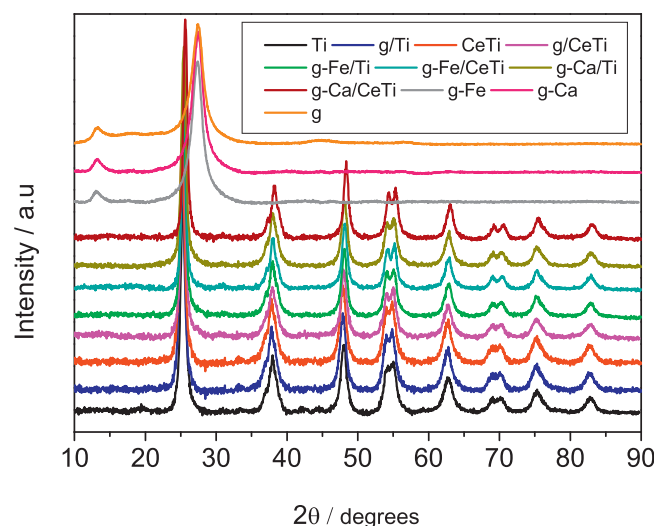


Fig. 1. XRD patterns of the references and samples.

Table 3
Size, microstrain and TiO₂ anatase cell parameters of the samples.^a

Sample	Size (nm) TiO ₂	Microstrain $\langle \xi^2 \rangle^{1/2} (\times 10^{-3})$ TiO ₂	TiO ₂ Anatase Cell parameters (Å)	
			a = b	c
Ti	12.1	2.08	3.789	9.481
g/Ti	12.0	2.06	3.790	9.480
CeTi	13.7	1.97	3.794	9.497
g/CeTi	13.4	1.97	3.791	9.493
g-Fe/Ti	12.0	2.05	3.791	9.493
g-Fe/CeTi	12.5	2.08	3.793	9.496
g-Ca/Ti	12.4	2.08	3.791	9.493
g-Ca/CeTi	13.1	1.97	3.791	9.493

^a Standard error: size 0.5 nm, cell parameters 0.003 Å.

Table 4
C1s and N1s XPS fitting results for samples. Binding energies (Electronvolts) and species concentration (in parenthesis percentage over total) are presented.

	g	g-Fe	g-Ca	g/Ti	g/CeTi	g-Fe/Ti	g-Fe/CeTi	g-Ca/Ti	g-Ca/CeTi
C1s									
C—C (%)	284.6 (10.1)	284.6 (11.1)	284.6 (11.4)	284.6 (53.2)	284.6 (54.0)	284.6 (52.2)	284.6 (51.7)	284.6 (52.8)	284.6 (53.7)
(C) ₃ —N (%)	286.2 (7.3)	286.2 (6.5)	286.1 (6.2)	286.1 (3.6)	286.1 (3.4)	286.1 (3.5)	286.1 (3.2)	286.2 (3.7)	286.2 (3.6)
C—N—C (%)	287.6 (82.6)	287.8 (82.4)	287.8 (82.1)	287.8 (43.2)	287.8 (42.6)	287.8 (44.3)	278.7 (45.1)	287.8 (43.5)	278.5 (42.7)
N1s									
Pi—exc. (%)	403.4 (5.1)	403.8 (5.1)	403.6 (5.7)	404.0 (4.9)	403.9 (5.4)	404.0 (5.1)	403.9 (5.3)	404.0 (5.3)	403.9 (5.6)
N—H (%)	400.6 (13.7)	400.5 (12.8)	400.3 (12.3)	403.0 (15.6)	400.2 (12.5)	400.3 (15.3)	400.4 (15.8)	400.3 (15.6)	400.2 (15.3)
(C) ₃ —N (%)	399.2 (25.7)	398.9 (27.6)	398.8 (27.9)	398.9 (25.8)	399.1 (24.3)	398.9 (26.1)	398.7 (25.2)	398.9 (25.2)	398.5 (25.1)
C—N—C (%)	397.5 (55.5)	398.0 (54.5)	398.1 (54.1)	398.1 (53.7)	398.3 (57.8)	398.1 (53.5)	398.2 (53.7)	398.1 (53.9)	398.2 (54.0)

to some extent the main anatase phase. In fact, we see a moderate growth of the surface area (Table 2) and anatase particle size (Table 3). The relatively mild conditions of interaction of the ceria-titania and the carbon nitride entities is reflected in the constancy of all morphological properties presented in Tables 2 and 3. This holds independently of the presence of Ca or Fe species in the

carbon nitride phase. We would like to note the fact that XRD (similarly to Raman, see Ref. [19]) does not provide information about the ceria or carbon nitride components mainly due to their relatively low loading. The state of both surface components is however addressed with the help of other techniques (see below). We finally point out that carbon and/or ceria doping of anatase in the TiO₂

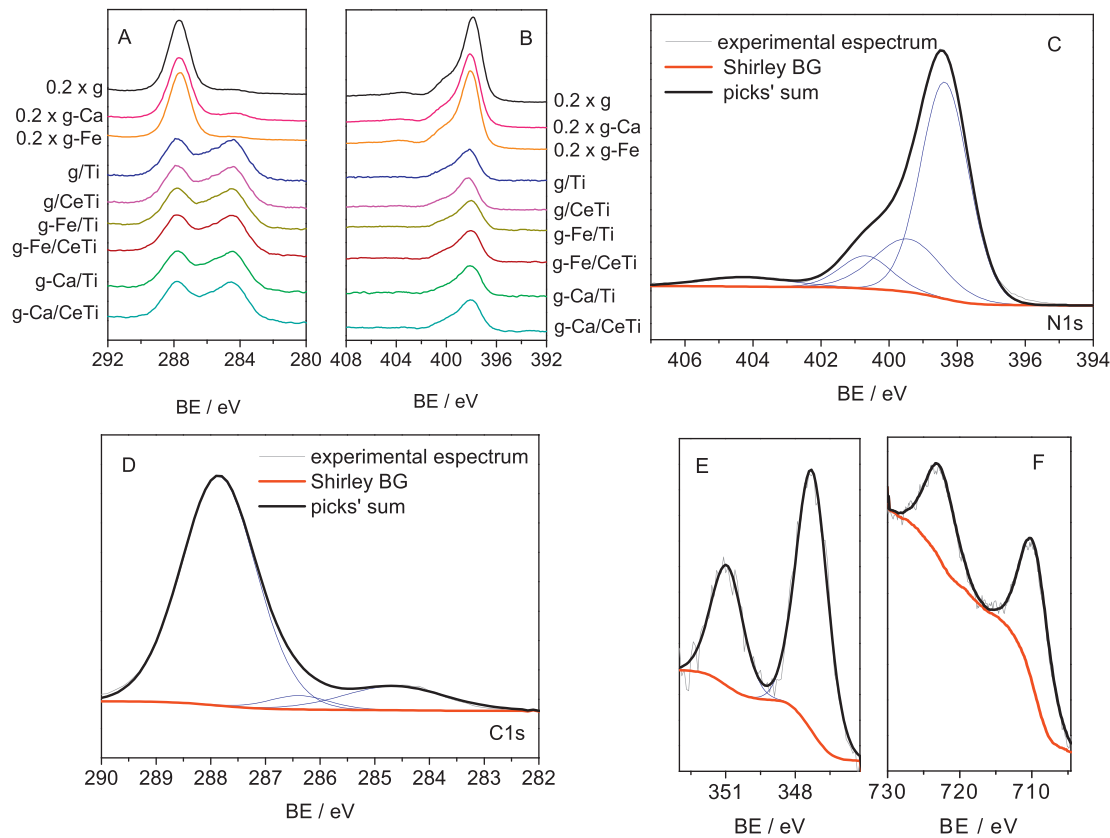


Fig. 2. C1s (A) and N1s (B) peaks for all samples and references containing carbon nitride. Representative example of the fitting procedure for the C1s (C), N1s (D) and Ca2p (E) XPS spectra of the g-Ca reference. The Fe3p (F) XPS spectrum is also presented for the g-Fe reference. Color labels in panels (E) and (F) are the same of (D) and (C).

or CeO_2 – TiO_2 containing samples does not occur to a significant extent as judged by the unperturbed cell parameters reported in Table 3.

To provide more information on the minor CeO_2 or $\text{g-C}_3\text{N}_4$ components in the catalysts as well as the M cationic species in the g-M/Ti references, we carried out a joint XPS and infrared study. Fig. 2A and B display XPS results of the carbon 1s (C1s) and nitrogen 1s (N1s) peaks in the ternary samples and single/binary references. A representative example of the fitting procedure to extract information for both C1s and N1s peaks is shown in Fig. 2C and D, respectively. A full summary of the fitting outcome is shown in Table 4. The remaining elements present in the samples were also studied by XPS and results described in Table 5, where no important differences were observed for the $\text{Ce}3d$, $\text{Ti}2p$, and $\text{O}1s$ peaks among g-M/Ti references and g-M/CeTi samples. This mainly concerns the oxidation states of Ce and Ti. XPS analysis is, therefore, the most significant technique providing structural and electronic information of the ceria component; it indicates (Table 5) the presence of ceria and titania oxides but interface effects produce a rather high Ce(III)/Ce(IV) atomic ratio of ca. 2.2, see Ref. [19] for further details. In short, the absence of significant differences in the ceria component can be noted when comparing all ceria-containing references/samples and the CeTi reference. Taking these results together with the fact that the method used for preparing all ternary systems employed the same CeTi material, we can conclude that Ce is essentially unaltered by the co-existence of carbon nitride species within the ternary samples.

The results of the C1s and N1s XPS peaks illustrated in Fig. 2A and B render information concerning the carbon nitride component. The fitting of experimental data depicted in Fig. 2 (Table 4) provide an evidence that the most important differences are detected in the C1s and more clearly when compared the g- C_3N_4 / g- C_3N_4 -M references and the TiO_2 -based catalysts. Three components were identified in the C1s XPS signal. As previously reported in similar systems, the C–C contribution shows a larger variation as a consequence of different importance of the spurious carbon-containing entities [20,28,32,34,61]. The other contributions exclusively ascribable to carbon nitride structural moieties, e.g., bridging carbons between aromatic moieties (C_3 –N) or at the aromatic rings (N –C–N), are also included in Table 4 [28,32,61]. They are essentially constant over the whole g-M/CeTi series and the corresponding reference systems. This indicates that rather minor differences are observed in the carbon nitride component when comparing the g/Ti reference with the g-M/Ti references and g-M/CeTi samples. This observation is also sustained by the N1s results presented in Fig. 2B and reported in Table 4, where no significant variation of the corresponding contributions is observed in both the binding energy and relative intensity, particularly in those contributions related to (C_3)–N and C–N–C moieties.

Corroboration of the XPS results concerning the carbon nitride state at the ternary systems was achieved using infrared spectroscopy (Fig. 3). In the case of the g- C_3N_4 reference, from high to lower wavenumbers N–H stretching vibration contribution(s) are present in the 3500 – 2500 cm^{-1} region. This is attributed to residual NH_x groups although the presence of adsorbed water molecules may also need to be considered [27,34,62]. In the 1600 – 1200 cm^{-1} region we can observe several contributions mostly associated with N–C stretching modes of heterocyclic compounds [61,63,64]. The same contributions can be observed in the composite, ternary catalysts and single and binary reference samples. Of course, in some regions, typically water or hydroxyl related ones, they overlap with intrinsic titania contributions. The region below ca. 1600 cm^{-1} displays, however, clear carbon nitride-like fingerprints in the composite catalysts. Specifically, in the 1600 – 1000 cm^{-1} region, although some of the bands differ for the composites and the

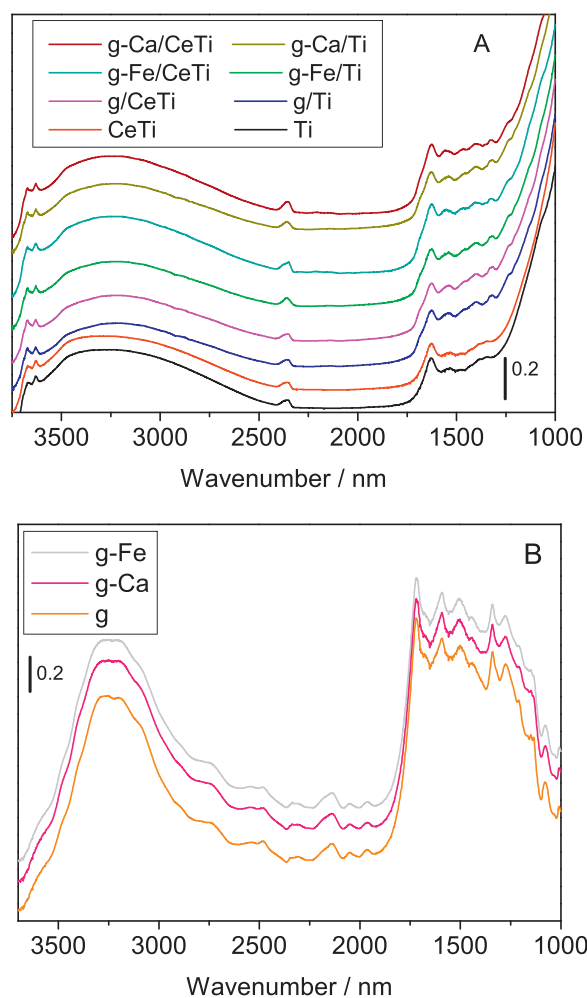


Fig. 3. FTIR spectra of the Ti, g-Ti, g-M/Ti and g-M/CeTi samples (A) and g and g-M references (B).

g- C_3N_4 reference, the general similarity of the corresponding vibrational modes indicates that the carbon nitride component preserves its main structural characteristics in the g-M/CeTi samples with respect to the corresponding single/binary references. The stability of the ceria and carbon nitride surface species was previously addressed and here we use IR to provide further evidence of the absence of significant differences when comparing the g-M/CeTi systems with the g/Ti reference in the specific case of the g- C_3N_4 component.

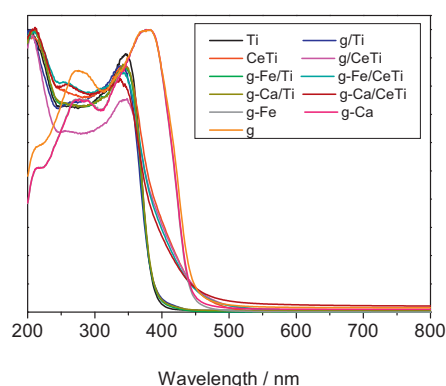


Fig. 4. UV-vis spectra of the TiO_2 -containing references and samples.

Table 5

Ca, Fe, Ce, Ti and O XPS fitting results (Electronvolt) for the samples.

Sample	Ca or Fe2p _{3/2}	Ce3d _{3/2} (u''')	Ce3d _{5/2} (v''')	Ce ³⁺ /Ce ⁴⁺	Ti2p _{3/2}	O1s
Ti	–	–	–	–	458.1	529.5
g-Ca	347.3	–	–	–	–	–
g-Fe	710.3	–	–	–	–	–
CeTi	–	916.6	898.5	2.2	458.3	529.6
g/Ti	n.d.	–	–	–	458.1	529.4
g/CeTi	–	916.6	898.5	2.3	458.2	529.4
g-Fe/Ti	n.d.	–	–	–	458.2	529.4
g-Fe/CeTi	n.d.	916.6	898.4	2.3	458.2	529.6
g-Ca/Ti	n.d.	–	–	–	458.2	529.4
g-Ca/CeTi	n.d.	916.6	898.5	2.2	458.2	529.6

n.d.: not determined (below detection limit). The Ce³⁺/Ce⁴⁺ ratios is estimated as described in ref. 19.

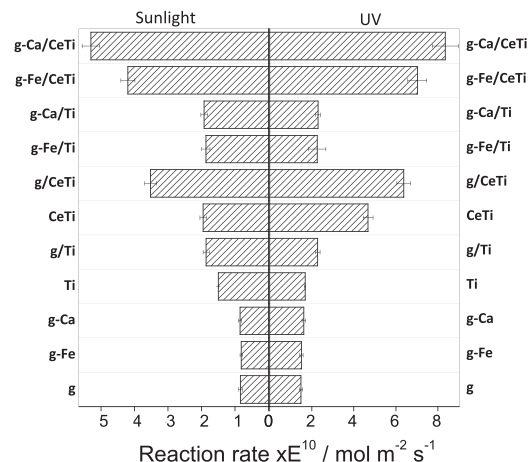
We used XPS to study the chemical state of the M cations in the binary g-M references. Note that their expected content in the Titania-containing reference materials and composite catalysts do not allow their detection and analysis by XPS. The Ca and Fe signals obtained in the above mentioned g-M/Ti references are displayed in Fig. 2E and F, respectively. Ca is obviously in a +2 state with 2p_{3/2} peak at the characteristic binding energy of 347.2 eV [65]. In the case of Fe, the binding energy presented in Table 5, 710.3 eV, indicates a dominant +2 state [65]. Both cations are thus present at the g-M references as a consequence of their interaction with the carbon nitride component, presumably through electrostatic forces [66].

The optical properties of the samples were examined using UV–Visible spectroscopy. In Fig. 4 we plotted the g-M/CeTi and corresponding reference systems spectra. The spectra are dominated by the titania component in the shorter wavelength region, displaying the characteristic intensity decay for a band gap energy of ca. 3.20 eV (Table 2). The presence of CeO₂ in the CeTi reference slightly decreases (ca. 0.23 eV) the band gap and modifies the spectrum shape in the visible region (Fig. 4). The decrease of the band gap energy is mostly attributable to a quantum nanostructural effect at the anatase phase [67] due to the complete absence of doping effects [19,20]. This nanostructural effect would be in turn related to surface effects exerted by the species present at the anatase surface as other contributions concerning size/shape/morphology changes (with respect to the bare titania reference sample) would be rather modest according to Table 2. The subsequent addition of the g-C₃N₄ (with or without Ca or Fe) component alters light absorption properties and band gap energy rather modestly. The changes of ca. 0.1 eV are thus presented in Table 2. In spite of the well-documented g-C₃N₄ light absorption capability in the UV and visible regions (34,61), its effect on the estimated band gap (i.e. UV region) of the g-M/CeTi catalysts is unnoticeable due to its limited content in the ternary systems. The results would indicate that the absorption properties in the visible region (above the one dominated by the titania band gap) are dominated by the CeO₂ component but with a non-negligible contribution (mainly visible in Fig. 4 around 400–500 nm) from the carbon nitride component.

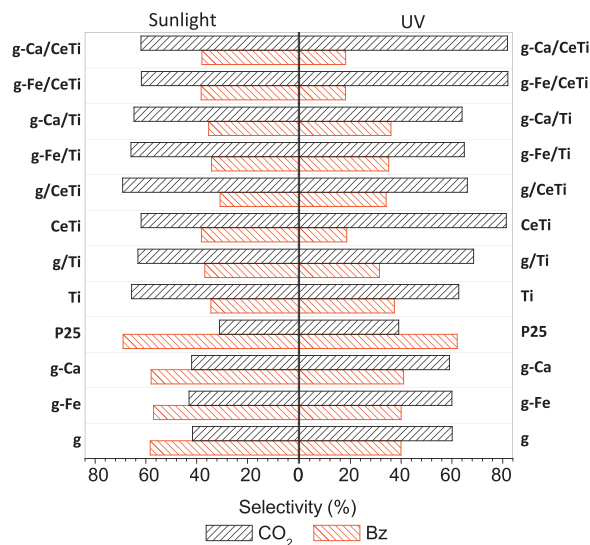
Finally, we note that the primary particle size of anatase, as detected by XRD, the shape of the IR spectra and thus the carbon nitride component as well as band gap calculations in used g-M/CeTi samples (results not shown) only display variations within experimental error, indicating the stability of the g-M/CeTi samples under reaction conditions.

3.2. Photoactivity

The photochemical performance of the obtained materials in elimination of toluene under UV and sunlight-type illumination is reported in Fig. 5. The figure evidences the high activity presented by the composite systems: in fact, even our microemulsion-prepared titania sample improves the Evonik P25 reference upon

**Fig. 5.** Surface-area-normalized reaction rate for toluene photo-oxidation under UV and sunlight-type illumination conditions.

both illumination conditions here tested. Note also that a CeO₂ reference obtained by microemulsion and calcined at the same temperature of our samples provided a toluene photo-elimination rate one order of magnitude inferior to the titania reference (see refs. [68,69] for details). Focusing now on the binary g/CeTi reference, we can see that both ceria and carbon nitride have a positive effect with respect to the titania reference. We previously analyzed this issue in the case of the binary g-Ti and CeTi systems [19,21,34]

**Fig. 6.** Selectivity toward benzaldehyde and CO₂ production under UV and sunlight-type illumination conditions. Standard error: ±6%.

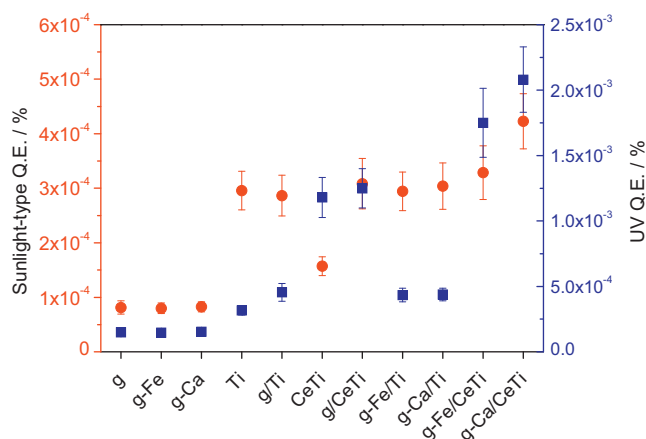


Fig. 7. Quantum Efficiency values for toluene photo-oxidation under UV and Sunlight-type illumination conditions.

as well as in the ternary g/CeTi materials [42], observing in the latter case simple, additive effects for the g and Ce component contributions to the photoactivity. In the present case, the addition of cationic species to the ternary g/CeTi system has a slightly positive effect in the case of Fe, whereas a more evident positive influence is observed in the case of Ca for all the illumination conditions tested.

Here we will analyze the photocatalytic properties in terms of calculating the true quantum efficiency, which considers both the effect of photon absorption by the photocatalysts as well as the chemical selectivity characteristic of each sample. The full calculation of the $e^{a,s}$ is detailed in the Appendix A section and requires calculation on a cylindrical geometry and thus two independent geometrical variables. The results under UV and sunlight-type illumination are presented in the Appendix B Figs. A2 and A3. These figures indicate the same geometrical behavior and thus differences between samples can be represented by a single number, the average value of $e^{a,s}$. Quantum efficiency calculations require the $e^{a,s}$ calculation as well as the measurement of the selectivity of the reaction. In the case of toluene photo-oxidation, only benzaldehyde and CO₂ are observed as the reaction products [19,20,34,59,70,71]. The production of such chemical species requires, according to the literature, an average of 1 and 4 holes for benzaldehyde and CO₂, respectively [19,20,13,70,71]. The ratio between the number of charge species used to produce these two chemical molecules is in any case an important parameter to obtain the accurate measurement of the quantum efficiency behavior throughout the sample series. Selectivity data for g-Mn/CeTi samples and single/binary reference systems is presented in Fig. 6. Briefly we mention that the ternary materials display modest changes in selectivity to mineralization with respect to single and binary reference systems. Such effect is positive (i.e. increasing mineralization) and is more profound in the presence of Fe or Ca and under UV illumination.

The results of the quantum efficiency calculation for all the illumination conditions employed in this work are displayed in Fig. 7. In the case of UV light and taking titania as a reference, the addition of ceria (e.g., CeTi) seems to have the highest impact on the quantum efficiency, with a relatively small influence of the carbon nitride component (g/Ti). This improvement occurs without significant changes in selectivity (Fig. 6) and is thus directly ascribable to an enhancement of the chemical efficiency per photon which origin will be analyzed below with the help of luminescence and TRMC spectroscopies. We note that the enhancement of photoactivity of titania by carbon nitride has been previously shown by many authors [28,34,32,61,63] but, when measured as true quantum efficiency, this positive effect is of relative modest significance

[34,42]. More importantly, we can see an increase in the quantum efficiency by 40 % in the Fe case and a more pronounced 66 % in the Ca case as compared to the g/CeTi system. Very minor changes in absorbance (Fig. 4) and modest modification of selectivity (Fig. 6) between Fe and Ca promoted ternary systems indicate some superior influence of the photon handling properties in the case of Ca. Such increase of the quantum efficiency does not occur in the g-M/Ti references with respect to g/Ti, being thus characteristic of the ternary system.

For the sunlight illumination conditions and taking Ti as a reference, we can detect a positive or negative effect in the presence of carbon nitride and ceria in their respective binary g/Ti and CeTi reference samples. We note that the contribution of selectivity to the quantum efficiency values is rather modest as compared with the Ti reference in presence of g-C₃N₄ or ceria (Fig. 6). Thus, the combined effect of selectivity (production of CO₂ requires a larger number of charge carriers) and, particularly, the strong absorption properties of ceria in the visible electromagnetic region are responsible for the more important decrease of the quantum efficiency in the presence of the lanthanide oxide (Fig. 7). In the case of the ternary systems and choosing g/CeTi as the adequate reference, we see again positive effects, more modest in the Fe (10%) than the Ca (41%) case. This is qualitatively similar to the UV case, likely indicating the importance of such contribution to the photoactivity obtained upon sunlight excitation. Again, minor changes in absorbance (Fig. 4) and selectivity (Fig. 6) point towards significant effects in charge handling properties in the case of Ca and less profound for Fe. As observed under UV illumination, this phenomenon only occurs in the ternary system, with minimal changes observed in g-M/Ti reference samples with respect to g/Ti.

3.3. Photoluminescence and TRMC

To interpret on a more detailed basis the physical origin of the photocatalytic behavior of g-M/CeTi samples, we carried out photoluminescence experiments under both UV and visible light excitation conditions. The corresponding UV experimental results are presented in the two panels of Fig. 8. UV excitation at 280 nm allows scanning all potential de-excitation channels of the titania, the main component of the g-M/CeTi materials. Below 620 nm the photoluminescence of titania dominated (as here is the main component) samples display the presence of two or three peaks [72–74]. We note that above such threshold, photoluminescence peaks are less important to generate photo-chemistry and are always related to presence of defective Ti (interstitial or lattice) states [75]. Transitions below 620 nm are classified into two groups, corresponding to high-energy (sometimes called green) and low energy (red) de-excitation channels. As it is well-known, titania demonstrates rather small photoluminescence intensity due to the indirect nature of this semiconductor [72–74]. After UV excitation the g-C₃N₄ reference shows, on the other hand, a broad band centered at ca. 440 nm with substantial photoluminescence intensity, as previously observed by several authors [34,61,76].

In the binary g-Ti and CeTi systems, the photoluminescence properties are modified as compared to the main titania component. In both cases new de-excitation channels, inherent to the binary (and not to the single components) have been observed in our previous works [19,34]. For the carbon nitride this de-excitation channel withdraws electrons from titania and annihilates them with holes from the carbon nitride (increasing photoluminescence signal with respect to pure titania) while in presence of ceria electrons from titania are captured at the ceria-titania interface by anion vacancies (decreasing photoluminescence signal with respect to titania). In spite of the different chemical nature of the surface species, both species essentially favor the capture of electrons from TiO₂ with involvement of anion vacancies in the case of

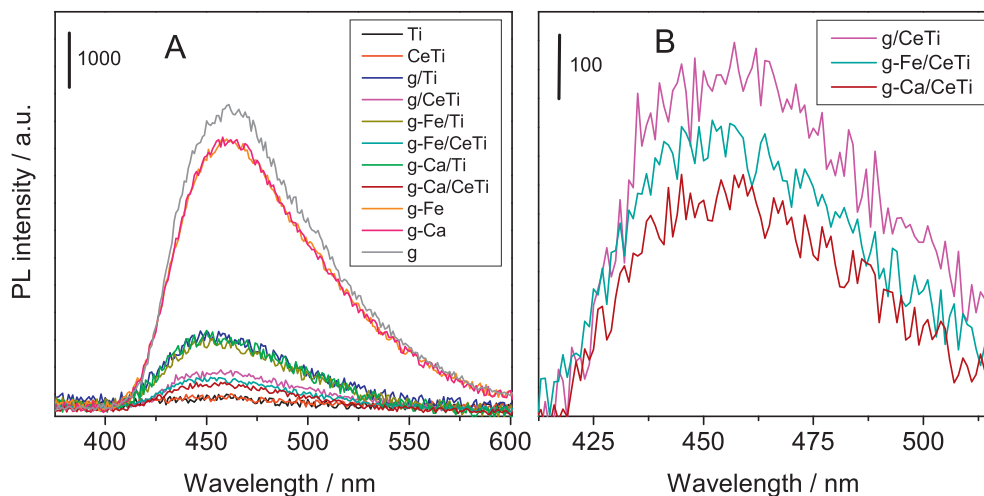


Fig. 8. Photoluminescence spectra of the references and samples. $\lambda_{\text{ext}} = 280$ nm. (A) All samples. (B) Expanded view concerning g/CeTi, g-Fe/CeTi and g-Ca/CeTi.

ceria and the annihilation process in the case of the carbon nitride [19,34,77].

The g-M/CeTi ternary systems behavior is better illustrated in the right hand panel of Fig. 8. The luminescence intensity is always lower than the one of the g/CeTi reference and decreases in the order Fe > Ca. Note that a direct comparison of photoluminescence intensities among the three samples mentioned directly reflects variations in the de-excitation phenomenon as the absorption properties of the samples are rather similar (see Fig. 4), as expected by their almost equal chemical/morphological/structural composition/characteristics. The photoluminescence intensity behavior through the series is a strong indication that the presence of these two cations may positively alter the recombination of charges, diminishing it if compared with the g/CeTi reference system.

The case of visible light excitation (excitation at 420 nm) is illustrated in Fig. 9. Titania renders, as expected, rather low intensity while the g-C₃N₄ reference shows rather high one [71–76]. Under visible light excitation there are, as already described under UV illumination conditions, new pathways for de-excitation, characteristic for the binary g/Ti and CeTi system when compared against their single constituents [21,34]. As in the previous case, the most interesting result coming from the photoluminescence variation

within ternary systems is illustrated in the right hand panel of Fig. 9. The same behavior observed under UV illumination becomes apparent; both Fe and Ca containing solids showed decreasing intensity with respect to the g/CeTi reference, and in the g/CeTi > g-Fe/CeTi > g-Ca/CeTi order.

The photoluminescence study shows therefore similar UV and visible light excitation trends that are fully in line with the quantum efficiency values presented in Fig. 7. This fact indicates that the dominant factor in the different photochemical behavior observed in the presence of Fe or Ca at ternary systems is related to charge recombination phenomena. Although the exact mechanism by which this operates is different under UV and visible light as well as varies with the surface species chemical nature [19,21,34,42,71–76], the overall result is a positive influence on the photocatalytic activity; as mentioned, Fe has a slightly positive effect and a more evident positive effect is observed in the case of Ca.

TRMC signals normalized by the amount of light absorbed by the films for the Ca-containing series of samples were used to further interpret the photocatalytic quantum efficiency results. The main differences among the samples concern the intensity of the signals, directly related to the electron mobility assuming that the

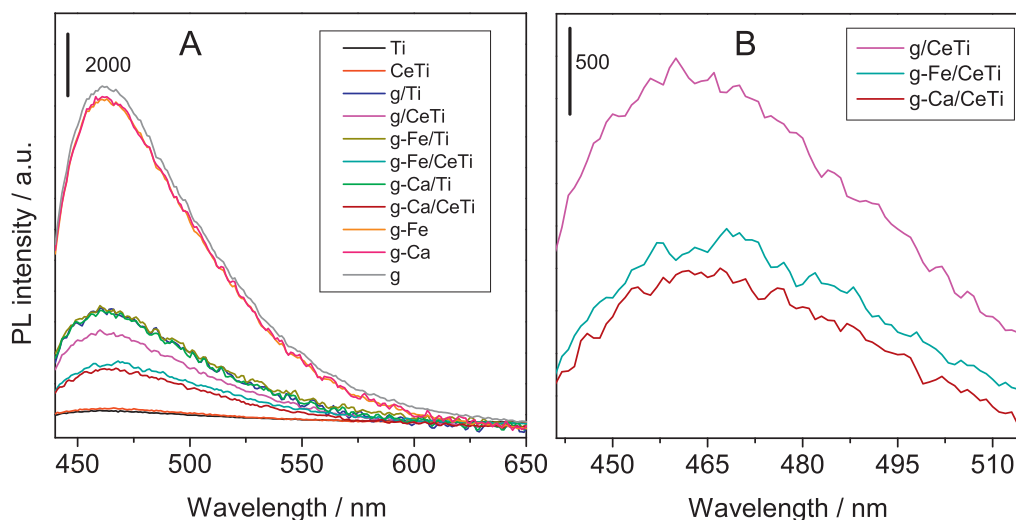


Fig. 9. Photoluminescence spectra of the references and samples. $\lambda_{\text{ext}} = 420$ nm. (A) All samples. (B) Expanded view concerning g/CeTi, g-Fe/CeTi and g-Ca/CeTi.

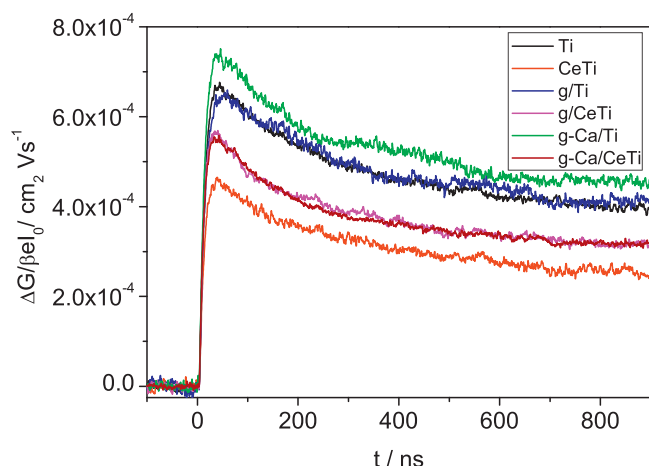


Fig. 10. MW-Intensity normalized photoconductivity transients. $\lambda_{exc} = 340$ nm.

charge generation efficiency values are equal [78]. Rather similar trends are observed under UV and visible light excitation. Although the electron capture by g and Ce within the binary g/Ti and CeTi systems is supported by the photoluminescence data, lifetimes of the photogenerated mobile charges are nearly identical for all the materials. A small variation of signal intensities is noted. The signal intensity is slightly lower in the case of CeTi as compared to g/Ti and titania itself. While both additives should have electron withdrawing properties, ceria is reported to be more effective [42]. However, one would expect a drastic change in lifetimes in case charge transfer from titania occurs [79]. This was not observed presumably due to the dominant molar fraction of titanium dioxide. As a bulk analysis technique, TRMC averages over the whole composite material while only a small fraction of titania experiences changes of the electronic properties associated with the intimate contact between TiO_2 and the other constituents of the binary and ternary systems. The electronic nature of the interactions between TiO_2 and the other additives is more apparent in the case of the photoluminescence spectroscopy as the dominant anatase phase does not display a substantial emission. The TRMC traces are dominated by the mobile charges in the bulk of TiO_2 and since g, Ce and M and are not integrated in the TiO_2 lattice and are present in low quantities the impact of these additives on the mobile charge carriers' lifetime was not detected in Figs. 10 and 11.

The photocatalytic effect of ceria and carbon nitride species present at the surface of a main titania phase is thus favored in presence of cations like Fe or Ca. The magnitude of the positive

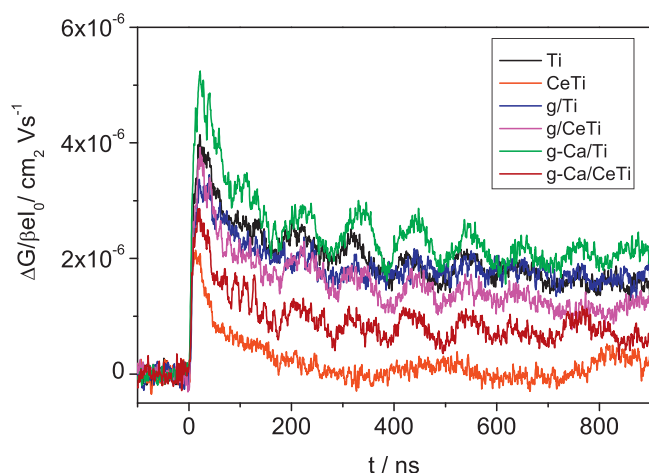


Fig. 11. MW-Intensity normalized photoconductivity transients. $\lambda_{exc} = 420$ nm.

effect depends on the intrinsic electronic properties of the cation and may be related to its ability to capture charge carrier species at a local level (i.e. when the cation is near and/or in contact with the titania surface), a fact supported by the previously presented analysis. A role of such cations in multi-step electron capture processes, relevant to activate oxygen species [80], may justify the better performance of Ca^{2+} vs. Fe^{2+} . This phenomenon would require the presence of localized states near the conduction band of the main titania component to handle electrons in such a way that an optimum trapping by oxygen can be achieved. This hypothesis needs however further work to assess its catalytic/kinetic significance.

4. Conclusions

The preparation of ternary systems where a metal-loaded carbon nitride and ceria species co-exist at the surface of a dominant titania-anatase phase was carried out with a combination of microemulsion and wet impregnation methods. The study focused on analyzing the effect of minute concentrations (at the $10^{-2}\%$ molar level) of cations located at the carbon nitride phase in the overall activity of a ternary system comprised of ceria, carbon nitride and the dominant anatase phase.

Finally, the UV and sunlight-driven performance of catalysts in the photooxidation of toluene was evaluated in terms of reaction rate and selectivity. By calculation of the true quantum efficiency of toluene photooxidation under all illumination tested, we observed that the co-existence of ceria and carbon nitride at anatase has a positive photocatalytic effect which is boosted in presence of the cationic species. The increase of activity is relatively mild for Fe cations and is more significant in presence of Ca, maintaining such trend irrespectively of the illumination conditions. The enhanced performance is unique for the ternary system, as it does not occur to a significant extent in the absence of ceria, and is affected by the chemical nature of the cationic species. Electrode-less conductivity measurements did not detect substantial changes in photogenerated charge carrier lifetimes, while photoluminescence studies provide strong evidence that such general enhancement of the photoactivity is directly linked to the influence of cations on the recombination of charge carrier species. We thus detected a measurable chemical effect of a cation species present at the level of traces (not detectable by chemical analysis) in the catalyst formulation.

Acknowledgements

A. Kubacka and M.J. Muñoz-Batista thank MINECO (Spain) for support thought, respectively, the postdoctoral “Ramón y Cajal” and predoctoral FPI programs. M.J.M-B. also wants to thank MINECO for a grant to visit Delft University (EEBB-I-14-08086). Financial support by MINECO (projects CTQ2010-14872/BQU and ENE2013-46624-C4-1-R) and Dutch National Research School “Combination Catalysis Controlled by Chemical Design” (NRSC-Catalysis) are gratefully acknowledged.

Appendix A.

(A1) Calculation of Quantum efficiency

The Quantum efficiency (Q.E.) of a photochemical reaction under UV and Sunlight-type irradiation can be determined from the reaction rate and the superficial rate of photon absorption according to Eq. A1.

$$\text{Q.E.}(\%) = \frac{\text{Reaction Rate (mol m}^{-2} \text{ s}^{-1})}{\text{Photon Rate (Einstein m}^{-2} \text{ s}^{-1})} \times 100 \quad (\text{A1})$$

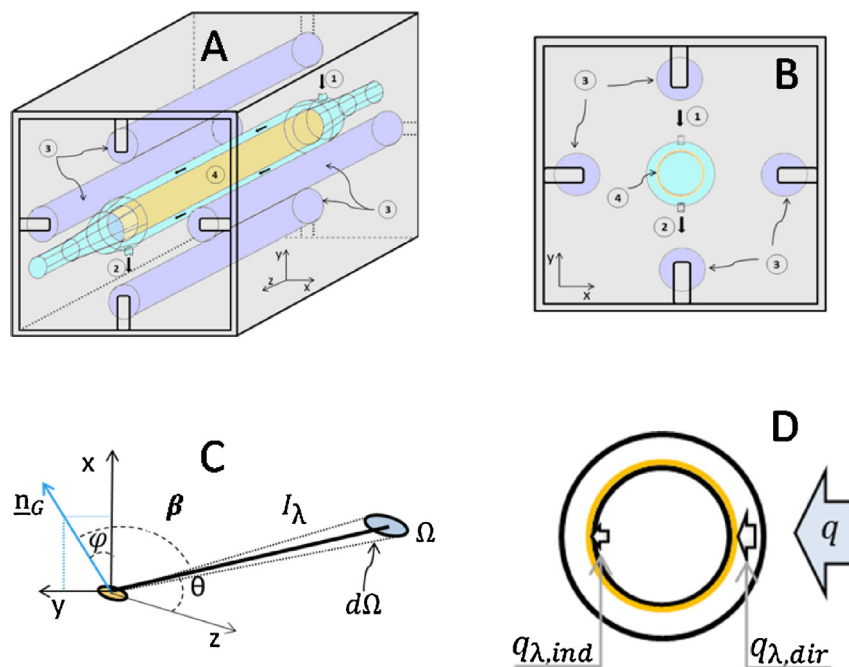


Fig A1. (A) Scheme of the photocatalytic reactor, (B) Side section view of the photocatalytic annular reactor, (1) gas inlet, (2) gas outlet, (3) lamps, (4) catalyst sample. (C) Coordinate system adopted for the reactor-lamps system and (D) Radiation fluxes scheme on the sample film.

To define the denominator of this equation, we first evaluate the local net superficial rate of photon absorption ($e^{a,s}$) of the samples (Details in Appendix B). In addition, it is necessary to consider the selectivity of the toluene photooxidation (Eq. A2) as two different molecules, benzaldehyde and carbon dioxide, are obtained in the reaction. This correction factor (γ) accounts for the number of

charge carrier species (and in turn photons) necessary to produce one molecule of a specific product and requires the measurement of the reaction selectivity.

$$\gamma_{TOL} = \sum_i n_i S_i \quad (A2)$$

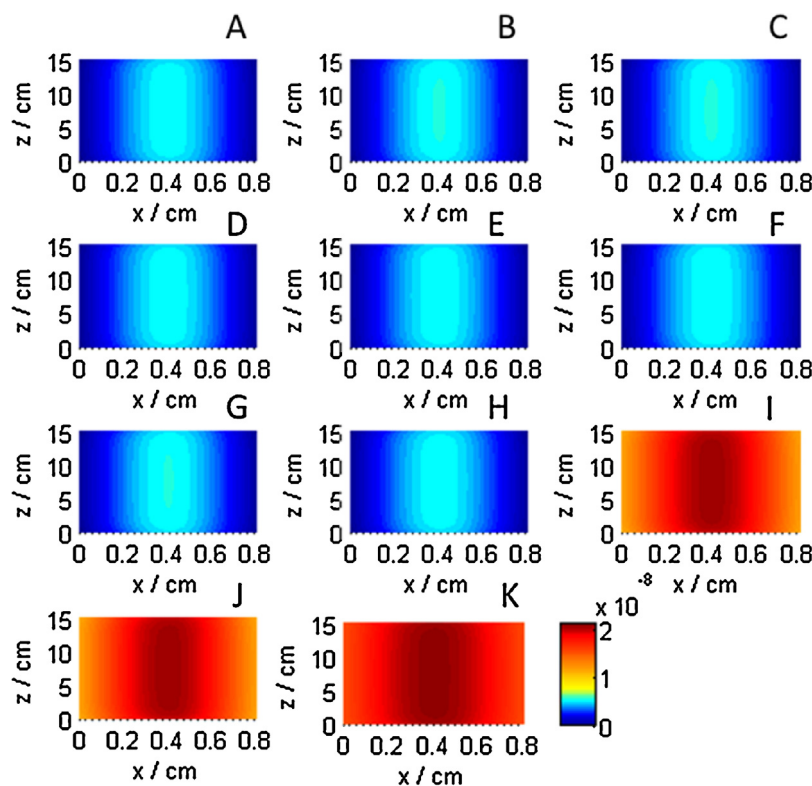


Fig A2. Local superficial rate of photon absorption ($\text{Einstein cm}^{-2} \text{s}^{-1}$) under UV irradiation. (A) Ti, (B) CeTi, (C) g/Ti, (D) g/CeTi, (E) g-Fe/Ti, (F) g-Ca/Ti, (G) g-Fe/CeTi, (H) g-Ca/CeTi, (I) g-Fe, (J) g-Ca and (K) g.

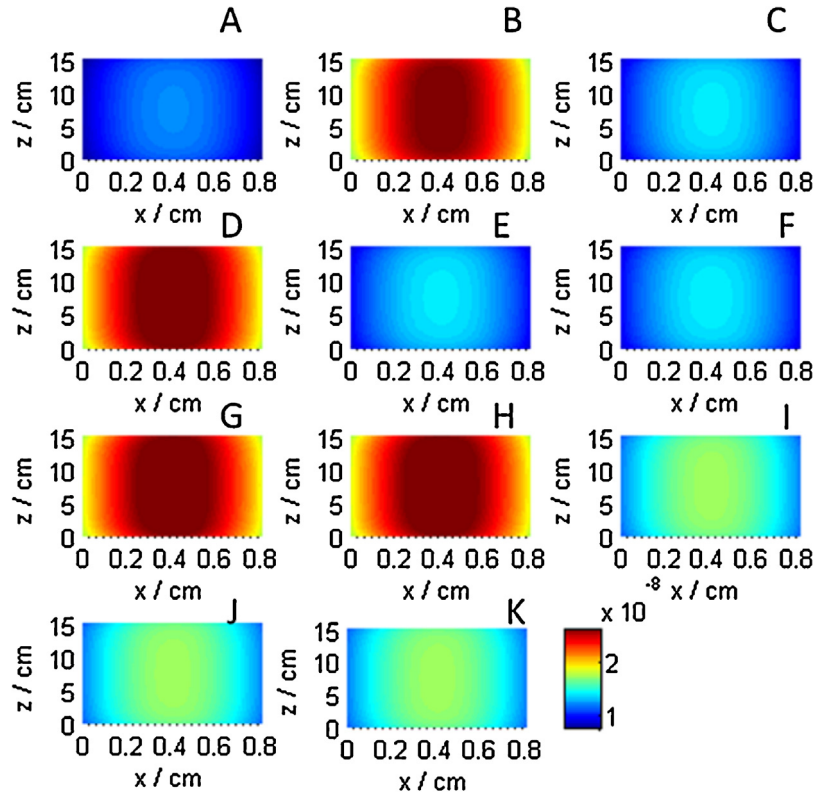


Fig A3. Local superficial rate of photon absorption ($\text{Einstein cm}^{-2} \text{s}^{-1}$) under sunlight-type irradiation. (A) Ti, (B) CeTi, (C) g/Ti, (D) g/CeTi, (E) g-Fe/Ti, (F) g-Ca/Ti, (G) g-Fe/CeTi, (H) g-Ca/CeTi, (I) g-Fe, (J) g-Ca and (K) g.

Where i runs over all products of the reaction, S_i is the fractional selectivity to product i , and n_i is the inverse of number of charge carrier species required to obtain the specific i product.

Appendix B.

(A3) Calculation of the $e^{a,s}$ coefficient

In order to compute the UV and Sunlight-type radiation field we adopted the three-dimensional source with superficial emission model and the ray-tracing computational method (13). Fig. A1 shows details of the reactor configuration and coordinate system used in this work. The spectral local superficial rate of photon absorption at each point on the reactor catalytic (x, y, z) surface is given by Eq. (A3) and is presented in Figs. A2 (UV) and A3 (Sunlight-type) for all catalysts here utilized.

$$e^{a,s}(x, y, z) = \sum_{L=4}^{\infty} \sum_{\lambda} \int_{\varphi_{\min}}^{\varphi_{\max}} \int_{\theta_{\min}}^{\theta_{\max}} I_{\lambda,L} \times \exp\left(-\frac{K_{\lambda,g} e_g}{\cos \beta}\right) \times \left[1 - \exp\left(-\frac{K_{\lambda,s} e_s}{\cos \beta}\right)\right] \sin^2 \varphi \left[\left(\frac{X_s - X_L}{R}\right) \cos \theta + \left(\frac{Y_s}{R}\right) \sin \theta\right] d\varphi d\theta + \sum_{L=4}^{\infty} \sum_{\lambda} \int_{\varphi_{\min}}^{\varphi_{\max}} \int_{\theta_{\min}}^{\theta_{\max}} I_{\lambda,L} \times \exp\left(-\frac{2K_{\lambda,g} e_g - K_{\lambda,s} e_s}{\cos \beta}\right) \times \left[1 - \exp\left(-\frac{K_{\lambda,s} e_s}{\cos \beta}\right)\right] \sin^2 \varphi \left[\left(\frac{X_s - X_L}{R}\right) \cos \theta + \left(\frac{Y_s}{R}\right) \sin \theta\right] d\varphi d\theta \quad (\text{A3})$$

The integration limits for the spherical coordinates ϕ and θ can be evaluated by the following Equations.

$$\varphi_{\min} = \tan^{-1}\left(\frac{X_L - X_s}{Y_L}\right) - \sin^{-1}\left(\frac{R_L}{(X_L - X_s)^2 + (Y_L)^2}\right) \quad (\text{A4})$$

$$\varphi_{\max} = \tan^{-1}\left(\frac{X_L - X_s}{Y_L}\right) + \sin^{-1}\left(\frac{R_L}{(X_L - X_s)^2 + (Y_L)^2}\right) \quad (\text{A5})$$

$$\theta_{\max}(\varphi) = \cos^{-1} \frac{-Zs}{(X_{Lm}(\varphi) - X_s)^2 + Y_{Lm}(\varphi)^2 + Zs^2} \quad (\text{A6})$$

$$\theta_{\min}(\varphi) = \cos^{-1} \frac{Z_L - Zs}{(X_{Lm}(\varphi) - X_s)^2 + Y_{Lm}(\varphi)^2 + Zs^2} \quad (\text{A7})$$

where:

$$X_{Lm}(\varphi) = X_L + (X_s - Y_L) \cos \varphi^2 + (Y_L)(\cos \varphi \sin \varphi) - \sin \varphi \sqrt{(R_L^2 - (Y_L \sin \varphi + (X_s - X_L) \cos \varphi)^2)} \quad (\text{A8})$$

$$Y_{Lm}(\varphi) = (Y_L) \cos \varphi^2 - (X_s - X_L)(\cos \varphi \sin \varphi) - \cos \varphi \sqrt{(R_L^2 - (Y_L \sin \varphi + (X_s - X_L) \cos \varphi)^2)} \quad (\text{A9})$$

Ω and \underline{n}_c are the angle between the ray trajectory and the film outwardly directed normal and unit vector outwardly directed normal to the catalytic film, respectively.

I is the radiation intensity and K and e are the equilibrium adsorption constant and thickness (values of $K_{\lambda,g} e_g$ (glass) and

$K_{\lambda,s}e_s$ (for each sample), were determined from spectral transmittance measurements), respectively. R is the inner radius reactor annulus, β is the angle between the ray trajectory and the film outwardly directed normal and λ denote dependency on wavelength. L , s , g refers to lamp, sample and glass, respectively.

References

- [1] L. Jing, W. Zhou, G. Tian, H. Fu, Chem. Soc. Rev. 42 (2013) 9509–9549.
- [2] A. Kubacka, G. Colón, M. Fernández-García, Chem. Rev. 112 (2012) 1555–1614.
- [3] J. Liu, J.Z. Zhang, Coord. Chem. Rev. 253 (2009) 3015–3041.
- [4] Z. Wang, Y. Liu, B. Huang, Y. Dai, Z. Lou, G. Wang, X. Xhang, X. Qin, Phys. Chem. Chem. Phys. 16 (2014) 2758–2774.
- [5] A. Kudo, Y. Miseki, Chem. Soc. Rev. 38 (2009) 253–278.
- [6] A. Primo, H. García, A. Corma, Phys. Chem. Chem. Phys. 13 (2011) 886–910.
- [7] M. Zou, Y. Kong, J. Wang, Q. Wang, Z. Wang, B. Wang, P. Fan, Spectrochim. Acta Part A 101 (2013) 82–90.
- [8] S. Parasupree, Y. Suzuki, S. Prisa-Art, S. Yoshikawa, J. Sol. St. Chem. 178 (2005) 128–134.
- [9] T. Tong, J. Zhang, B. Tian, F. Chen, D. He, M. Anpo, J. Colloid Interfaces Sci. 315 (2007) 382–388.
- [10] G. Li, D. Zhang, Y.C. Yu, Phys. Chem. Chem. Phys. 11 (2009) 3775–3782.
- [11] V. Stengl, S. Bakardejieva, N. Murafa, Mater. Chem. Phys. 114 (2009) 217–226.
- [12] H. Liu, M. Wang, Y. Wang, Y. Liang, W. Cao, Y. Su, J. Photochem. Photobiol. A 223 (2011) 157–162.
- [13] M.J. Muñoz-Batista, A. Kubacka, M.N. Gómez-Cerezo, D. Tudela, M. Fernández-García, Appl. Catal. B 140–141 (2013) 626–635.
- [14] Y. Wang, B. Li, C. Zhang, L. Cui, S. Kang, X. Li, L. Zhou, Appl. Catal. B 130–131 (2013) 277–284.
- [15] Y. Liu, P. Fang, Y. Cheng, Y. Gao, F. Chen, Z. Liu, Y. Dai, Chem. Eng. J. 219 (2013) 478–485.
- [16] P. Du, Z. Zhao, G. Chen, Chinese J. Environ. Eng. 7 (2013) 3933–3938.
- [17] A.A. Ismail, H. Bouzil, J. Colloid Interfaces Sci. 404 (2013) 127–134.
- [18] C. Karunakaran, P. Gomathisankar, ACS Sus. Chem. Eng. 1 (2013) 1555–1563.
- [19] M.J. Muñoz-Batista, M.N. Gómez-Cerezo, A. Kubacka, D. Tudela, M. Fernández-García, ACS Catal. 4 (2014) 63–72.
- [20] X. Sun, C. Li, L. Ruan, Z. Peng, J. Zhao, Y. Li, J. Alloy Compd. 585 (2014) 800–804.
- [21] M.J. Muñoz-Batista, M. Ferrer, M. Fernández-García, A. Kubacka, Appl. Catal. B 154–155 (2014) 350–359.
- [22] H. Eskandarloo, A. Badiei, M.A. Behnajadi, Ind. Eng. Chem. Res. 53 (2014) 7847–7855.
- [23] M.J. Muñoz-Batista, M.M. Ballari, A. Kubacka, A.E. Cassano, O.M. Alfano, M. Fernández-García, Chem. Eng. J. 255 (2014) 297–306.
- [24] M.J. Muñoz-Batista, M.M. Ballari, A.E. Cassano, O.M. Alfano, M. Fernández-García, A. Kubacka, Catal. Sci. Technol. 5 (2015) 1521–1531.
- [25] Z. Li, J. Seng, Y. Zhang, X. Li, Y. Yu, Appl. Catal. B 166–167 (2015) 313–319.
- [26] S. Luo, T.-D. Nguyen-Phan, A.C. Johnston-Peck, L. Barrio, S. Sallies, D.A. Arena, E. Fujita, J.A. Rodríguez, S.D. Senanayake, J. Phys. Chem. C 119 (2015) 2669–2679.
- [27] H. Yan, H. Yang, J. Alloy Compd. 509 (2011) L26–29.
- [28] S. Obregón, G. Colón, Appl. Catal. B 144 (2014) 775–783.
- [29] J. Wang, J. Huang, H. Xu, A. Qu, Int. J. Hydrogen Energy 39 (2014) 6354–6363.
- [30] Z. Huang, Q. Sun, L. v. Kangle, Z. Zhang, M. Li, B. Li, Applied Catalysis B 164 (2015) 420–427.
- [31] S. Zhou, Y. Liu, J. Li, Y. Wang, G. Jiang, Z. Zhao, D. Wang, A. Duan, J. Liu, Y. Wen, Appl. Catal. B 158–159 (2014) 20–29.
- [32] J. Yu, S. Wang, J. Low, W. Xiao, Phys. Chem. Chem. Phys. 15 (2013) 16883–16889.
- [33] C. Miranda, H. Mansilla, J. Yáñez, S. Obregón, G. Colón, J. Photochem. Photobiol. A 253 (2013) 16–24.
- [34] M.J. Muñoz-Batista, A. Kubacka, M. Fernández-García, Catal. Sci. Technol. 4 (2014) 2006–2015.
- [35] K. Shidharan, E. Jang, T.J. Park, Appl. Catal. B 142–143 (2013) 718–723.
- [36] X.-J. Wang, W.-Y. Yang, F.-T. Li, Y.-B. Xue, R.-H. Liu, Y.-J. Liao, Ind. Eng. Chem. Res. 52 (2013) 17140–17146.
- [37] F. Chang, J. Zhang, Y. Xie, C. Li, J. Wang, J. Luo, B. Deng, X. Hu, Appl. Surf. Sci. 311 (2014) 574–581.
- [38] N. Boohprokov, N. Wetchakon, D. Waxler, B. Inceesungrom, J. Coll. Int. Sci. 417 (2014) 402–409.
- [39] L. Zhang, D. Jing, X. She, H. Liu, D. Yang, Y. Lu, J. Li, Z. Zheng, L. Gou, J. Mater. Chem. A 2 (2014) 2071–2077.
- [40] Z. Huang, Q. Sun, K. Lv, Z. Zhang, M. Li, B. Li, Appl. Catal. B 164 (2015) 420–427.
- [41] Z. Tong, D. Yang, T. Xiao, Y. Tian, Z. Jian, Chem. Eng. J. 260 (2015) 117–125.
- [42] M.J. Muñoz-Batista, A. Kubacka, M. Fernández-García, Appl. Catal. B 164 (2015) 261–270.
- [43] M.J. Muñoz-Batista, A. Kubacka, M. Fernández-García, ACS Catal. 4 (2014) 4277–4288.
- [44] J. Mo, Y. Zhang, Q. Xu, Y. Zhu, J.J. Lamson, R. Zhao, Appl. Catal. B 89 (2009) 570–576.
- [45] A. Kubacka, G. Colón, M. Fernández-García, Catal Today 143 (2009) 286–292.
- [46] Y.W.S. Luo Tan, H.O. Seo, K.-D. Kim, M.J. Kim, N.K. Dey, Y.D. Kim, K.H. Choi, D.C. Lim, Catal. Lett. 130 (2010) 76–81.
- [47] A. Kubacka, M.J. Muñoz-Batista, R. Rachwalik, B. Bachiller-Baeza, M. Fernández-García, J. Catal. 309 (2014) 428–438.
- [48] G.E. Imoberdorf, A.E. Cassano, O.M. Alfano, H.A. Irazoqui, AIChE J. 52 (2006) 1814–1821.
- [49] L. Zhang, W.A. Anderson, Chem. Eng. J. 62 (2010) 1513–1519.
- [50] Q.L. Yu, M.M. Ballari, H.J.H. Brouwers, Appl. Catal. B 99 (2010) 58–65.
- [51] A.L. Zazueta, H. Destallais, G.L. Puma, Chem. Eng. J. 217 (2013) 475–482.
- [52] P.G. De Gennes, C. Taupin, J. Phys. Chem. 86 (1982) 2294–2303.
- [53] A. Kubacka, G. Colón, M. Fernández-García, Appl. Catal. B 95 (2010) 238–244.
- [54] S. Brunauer, P.H. Emmett, E. Teller, J. Am. Chem. Soc. 60 (1938) 309.
- [55] A. Le Bail, H. Duroy, J.L. Forquet, Mater. Res. Bull. 23 (1988) 447–452.
- [56] G.K. Williamson, W.H. Hall, Acta Metall. 1 (1953) 22–31.
- [57] J.E. Kroeze, T.J. Savenije, J.M. Warman, J. Am. Chem. Soc. 126 (2004) 7608–7618.
- [58] J.T. Carneiro, T.J. Savenije, G. Mul, Phys. Chem. Chem. Phys. 11 (2009) 2708–2714.
- [59] A. Fuerte, M.D. Hernández-Alonso, A.J. Maira, A. Martínez-Arias, M. Fernández-García, J.C. Conesa, J. Soria, G. Munuera, J. Catal. 212 (2002) 1–9.
- [60] A. Kubacka, B. Bachiller-Baeza, G. Colón, M. Fernández-García, Appl. Catal. B 93 (2010) 274–281.
- [61] G. Dong, Y. Xhang, Q. Pan, J. Qui, J. Photochem. Photobiol. C 20 (2014) 33–50.
- [62] G. Colón, M.C. Hidalgo, J.A. Navio, A. Kubacka, M. Fernández-García, Appl. Catal. B 90 (2009) 633–641.
- [63] J.S. Zhang, J.H. Sun, K. Maeda, K. Domen, P. Liu, M. Antonietti, X.Z. Fu, X.C. Wang, Energy Environ. Sci. 4 (2011) 675–678.
- [64] M. Xiong, L. Chen, Q. Yuan, J. He, S.-L. Luo, C.T. Au, S.-F. Yin, Dalton Trans. 43 (2014) 8331–8337.
- [65] C.D. Wagner, W.M. Riggs, L.E. Davis, J.F. Moulder, Handbook of X-ray Photoemission Spectra, in: G.E. Muilenber (Ed.), Perkin-Elmer, Minnesota, 1976.
- [66] N. Zhang, M.Q. Yang, X.J. Xu, ACS Nano 8 (2014) 622–633.
- [67] M. Fernández-García, A. Martínez-Arias, J.C. Hanson, J.A. Rodríguez, Chem. Rev. 104 (2004) 4063–4105.
- [68] M.D. Hernández-Alonso, A.B. Hungria, A. Martínez-Arias, M. Fernández-García, J.M. Coronado, J.C. Conesa, J. Soria, Appl. Catal. B 50 (2004) 167–175.
- [69] M.D. Hernández-Alonso, A.B. Hungria, A. Martínez-Arias, J.M. Coronado, J.C. Conesa, J. Soria, M. Fernández-García, Phys. Chem. Chem. Phys. 6 (2004) 3524–3529.
- [70] J. Mo, Y. Zhang, Q. Xu, Y. Zhu, J.J. Lamson, R. Zhao, Appl. Catal. B 89 (2009) 570–577.
- [71] Y. Feng, L. Li, M. Ge, C. Gou, J. Wang, L. Liu, ACS Appl. Mater. Interf. 2 (2010) 3134–3142.
- [72] T. Tachikawa, T. Majima, J. Am. Chem. Soc. 131 (2009) 8485–8487.
- [73] X. Wang, Z. Feng, J. Shi, G. Jia, S. Shen, J. Zhou, C. Li, Phys. Chem. Chem. Phys. 12 (2010) 7083–7089.
- [74] C.C. Mercado, Z. Seeley, A. Bandyopadhyay, S. Bose, J.L. McHale, A.C.S. Appl. Mater. Interf. 3 (2011) 228–235.
- [75] E. Finnazi, C.D. Valentin, G. Pacchioni, J. Phys. Chem. C 113 (2009) 3382–3391.
- [76] S. Wang, C. Li, T. Wang, P. Zhang, A. Li, J. Wong, J. Mater. Chem. A 2 (2014) 2885–2891.
- [77] Z. Jin, N. Murakami, T. Tsubota, T. Ohno, Appl. Catal. B: Environ. 150–151 (2014) 479–486.
- [78] R. Katoh, A. Huijser, K. Hara, T.J. Savenije, L.D.A. Siebbeles, J. Phys. Chem. C 111 (2007) 10741–10746.
- [79] M.C. Fravventura, D.A. Siebbeles, T.J. Savenije, J. Phys. Chem. C 118 (2014) 7337–7343.
- [80] Y. Huoge, H. Irie, Y. Hosogi, Y. Kuroda, M. Miyauchi, K. Hashimoto, J. Phys. Chem. C 114 (2010) 16481–16487.